Letter

Real-time calibration of nuclear velocities in the dissociation of heteronuclear molecules in strong laser fields

Zhao-Han Zhang[1] and Feng He [1,2,*]

[1]*Key Laboratory for Laser Plasmas (Ministry of Education) and School of Physics and Astronomy, Collaborative Innovation Center for IFSA (CICIFSA), Shanghai Jiao Tong University, Shanghai 200240, China*
[2]*CAS Center for Excellence in Ultra-intense Laser Science, Shanghai 201800, China*

We design a strategy for the real-time calibration of nuclear velocities in ultrafast molecular reactions in strong laser fields by simulating the four-dimensional time-dependent Schrödinger equation. Taking HD^+ as the prototype, an attosecond pump pulse initiates the molecular dissociation, and the other time-delayed attosecond probe pulse, polarized in the plane perpendicular to the molecular axis, ionizes the dissociating HD^+. During the dissociation, two nuclei with different masses acquire different velocities, which imprint on the photoelectron kicked off by the probe pulse. The expected photoelectron momentum along the molecular axis can be used to precisely calibrate instantaneous nuclear velocities at ionization. This strategy works widely in general heteronuclear molecules and paves the way for making high-definition molecular movies.

With the advent of ultrafast laser technologies, making molecular movies with unprecedented time resolution has been considered by physicists in the ultrafast community [1,2]. By watching the molecular movie, one may understand the causality determined by electromagnetic interactions among particles in a microcosm, and further find ways to control the molecular processes, such as selectively breaking and forming molecular bonds [3–6]. Due to the simplicity of the target, H_2 and its isotopical molecules become preferential targets in experiment [5–13]. After the single ionization of H_2, the produced H_2^+ starts to breathe, i.e., the molecular bond stretches and shrinks periodically. To track the molecular vibration in the time domain, Ergler *et al.* [14] conceived the pump-probe experiment and reconstructed the time-dependent internuclear distance R using the relationship $KER = 1/R$ (atomic units are used unless stated otherwise), where KER is the kinetic energy release (KER) of Coulomb explosion fragments. Alternatively, the internuclear distance can be extracted by diagnosing the double-slit interference pattern in molecular ionization [15–19]. Since electrons and nuclei in H_2 are entangled, a photoelectron from H_2 or H_2^+ can be used to retrieve the nuclear dynamics [20,21].

To make molecular movies, it is not sufficient to only record the internuclear distance. The instantaneous nuclear velocity also requires identification. Especially for the molecular vibration within one period, stretching and shrinking may pass the same internuclear distance but the nuclei move oppositely. In the reconstruction of internuclear distance using the relationship of $KER = 1/R$, one has neglected the nuclear kinetic energy T_0 before the molecule breaks up. However, for a typical one-photon dissociation pathway of H_2^+, the vibrational velocity could be in the same order of magnitude

with the final velocity after the Coulomb explosion [12,22], and thus it is required to use $KER = 1/R + T_0$ to reconstruct the internuclear distance in order to make a high-definition movie.

In this Letter, we design a strategy to reconstruct the time-dependent bond length and nuclear velocity simultaneously. In the dissociation of heteronuclear diatomic molecules, such as HD^+, the momentum conservation law enforces the nuclei with different masses to acquire different magnitudes of velocities. If the molecule is ionized, the photoelectron will inherit the nuclear velocity in its momentum distribution. By detecting the electron-nuclei joint momentum spectrum (JMS) after ionization, the instantaneous internuclear distance and nuclear velocity can be extracted. To reveal such a process, we conceive an attosecond-pump–attosecond-probe strategy, as shown by Fig. 1, which can be performed with current advanced laser technologies [23,24]. Assuming HD^+ is aligned along the z axis, the first attosecond pulse, polarized along the z axis, is introduced to excite HD^+ from the ground state to its first excited electronic state, leading to molecular dissociation. During the dissociation, the nuclear velocity is inversely proportional to their masses. The other time-delayed attosecond pulse, which is circularly polarized in the x-y plane, is introduced to ionize the dissociating HD^+. The expected photoelectron momentum along the molecular axis is purely boosted by the asymmetric nuclear movement since the laser electric field of the probe pulse drives the electron movement in the x-y plane. Reversely, the expected photoelectron momentum along the molecular axis can be used to retrieve the nuclear velocities at ionization. We may point out that the polarization of the probe pulse can be arbitrary only if it is polarized in the x-y plane. Otherwise, any asymmetric factor of the laser field, for example, the carrier envelope phase, will induce an asymmetric electron momentum distribution, which blurs the asymmetry induced by the mass difference of two nuclei.
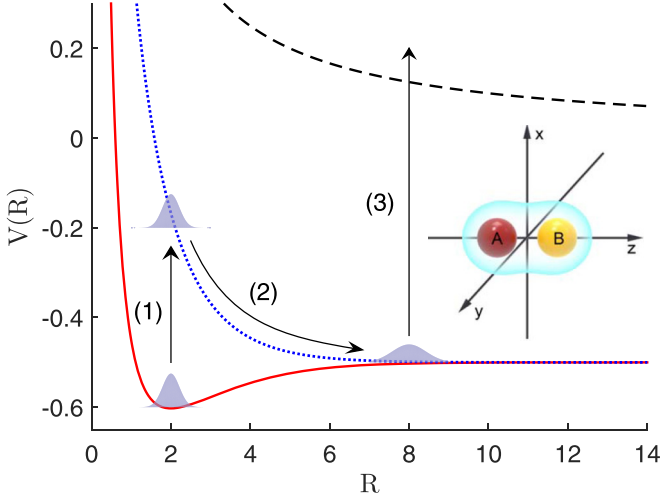
*fhe@sjtu.edu.cn

FIG. 1. Scheme of the pump-probe strategy in the dissociation-ionization process. The solid-red and dotted-blue curves are the potential energy curves of the two lowest electronic states of HD$^+$. The dashed curve represents the ionization threshold. The geometric configuration of the molecular system is presented in the lower right-hand corner. The internuclear motion is constrained along the z axis, while the electron is free to move in three dimensions. The nuclei in the left- and right-hand sides of the x-y plane are labeled as A and B, respectively. The first attosecond pulse excites HD$^+$ from the ground state to the first excited state, and then HD$^+$ starts to stretch, followed by ionization by another time-delayed attosecond pulse. These three processes are indicated by arrows marked with (1), (2), and (3), respectively. All quantities are in atomic units.

To simultaneously describe dissociation and ionization beyond the Born-Oppenheimer approximation (BOA), we numerically simulate a four-dimensional time-dependent Schrödinger equation (TDSE),

$$i\frac{\partial}{\partial t}\Psi(R, \rho, \varphi, z; t) = [H + W(t)]\Psi(R, \rho, \varphi, z; t), \quad (1)$$

where $\rho = \sqrt{x^2 + y^2}$, $\varphi = \arctan(y/x)$, and z are the electron coordinates, and R is the internuclear distance, as indicated in Fig. 1. The rotation of the molecule and the spin of the electron are neglected. The field-free Hamiltonian is

$$H = -\frac{1}{2\mu_e}\left(\frac{\partial^2}{\partial\rho^2} + \frac{1}{\rho}\frac{\partial}{\partial\rho} + \frac{1}{\rho^2}\frac{\partial^2}{\partial\varphi^2} + \frac{\partial^2}{\partial z^2}\right)$$
$$- \frac{1}{2\mu_n}\frac{\partial^2}{\partial R^2} + V_e(\rho, z, R) + \frac{1}{R}, \quad (2)$$

where $\mu_n^{-1} = m_A^{-1} + m_B^{-1}$ and $\mu_e^{-1} = (m_A + m_B)^{-1} + m_e^{-1}$ with m_A, m_B, and m_e the masses of nuclei and the electron. The nuclei-electron Coulomb potential $V_e(\rho, z, R)$ in Eq. (2) is written as

$$V_e(\rho, z, R) = -\frac{1}{\sqrt{\left(\frac{m_m}{m_n}\rho\right)^2 + \left(\frac{m_m}{m_n}z + \frac{m_B}{m_n}R\right)^2}}$$
$$- \frac{1}{\sqrt{\left(\frac{m_m}{m_n}\rho\right)^2 + \left(\frac{m_m}{m_n}z - \frac{m_A}{m_n}R\right)^2}}, \quad (3)$$

with $m_n = m_A + m_B$ and $m_m = m_A + m_B + m_e$. Note that the origin is placed at the center of mass (c.m.) of three particles such that the Coulomb centers appear at $-\frac{m_B}{m_m}R$ and $\frac{m_A}{m_m}R$. Putting the origin at either the total mass center or the nuclear mass center makes no observable difference for the results to be discussed. The laser-molecule interaction in the dipole approximation is expressed as

$$W(t) = \gamma_e E_x(t)\rho\cos\varphi + \gamma_e E_y(t)\rho\sin\varphi$$
$$+ \gamma_e E_z(t)z - \gamma_n E_z(t)R, \quad (4)$$

where the coefficients are $\gamma_e = 1 + 2m_e/m_n$, $\gamma_n = \mu_n(m_B^{-1} - m_A^{-1})$. The last term on the right-hand side of Eq. (4) hardly contributes to the concerned effects and actually can be neglected. The first attosecond laser field is expressed as

$$E_z(t) = E_1\sin^2(\pi t/\tau_1)\cos(\omega_1 t), \quad t \subset [0, \tau_1], \quad (5)$$

and the two components of the second attosecond laser field are expressed as

$$E_x(t) = E_2\sin^2[\pi(t - \Delta t)/\tau_2]\cos[\omega_2(t - \Delta t)],$$
$$t \subset [\Delta t, \Delta t + \tau_2],$$
$$E_y(t) = E_2\sin^2[\pi(t - \Delta t)/\tau_2]\sin[\omega_2(t - \Delta t)],$$
$$t \subset [\Delta t, \Delta t + \tau_2], \quad (6)$$

where ω_1 (τ_1) and ω_2 (τ_2) are the frequencies (durations) of the pump and probe pulses, and Δt is the time delay between two pulses.

In simulations, the wave function is expanded by a set of angular bases as

$$\Psi(R, \rho, \varphi, z; t) = \sum_{\Lambda=-\Lambda_0}^{\Lambda_0} u_\Lambda(R, \rho, z; t)\frac{e^{i\Lambda\varphi}}{\sqrt{2\pi}}. \quad (7)$$

In this Λ representation, the field-free Hamiltonian H is block-diagonal, while in the original φ representation, the laser interaction $W(t)$ is block-diagonal. For the remaining R, ρ, and z coordinates, we adopt the finite-difference (FD) representation on a three-dimensional equal-step grid. Throughout our study, we use a symmetric five-point FD format for nonboundary R, ρ, and z points while the boundary ones are treated via the same procedure as Ref. [4]. To save the efforts of solving large sparse linear systems, the Hamiltonian matrix is further decomposed into a tightly banded matrix by the split-operator technique [25], and the time evolution is efficiently performed by the Crank-Nicolson method [26]. The initial ground state is obtained by imaginary-time propagation [27]. After the laser pulse has vanished, we keep propagating the wave function for extra time in order to obtain the converged momentum distributions. The simulation box is big enough to hold all single-photon ionization events from the dissociative wave packet. Very few ionization events induced by the pump pulse or the multiphoton ionization by the probe pulse are absorbed by the mask function near the boundaries. As a consequence of few-photon ionization, only the first few Λ states are populated, thus the number of necessary angular bases is significantly reduced. The numbers of grid points for each variable are denoted by N_R, N_ρ, N_z, $2\Lambda_0 + 1$, and their grid steps are denoted by ΔR, $\Delta\rho$, Δz. We find that $\Delta R = 0.02$, $\Delta\rho = 0.25$, $\Delta z = 0.18$, $\Lambda_0 = 3$, $N_R =$
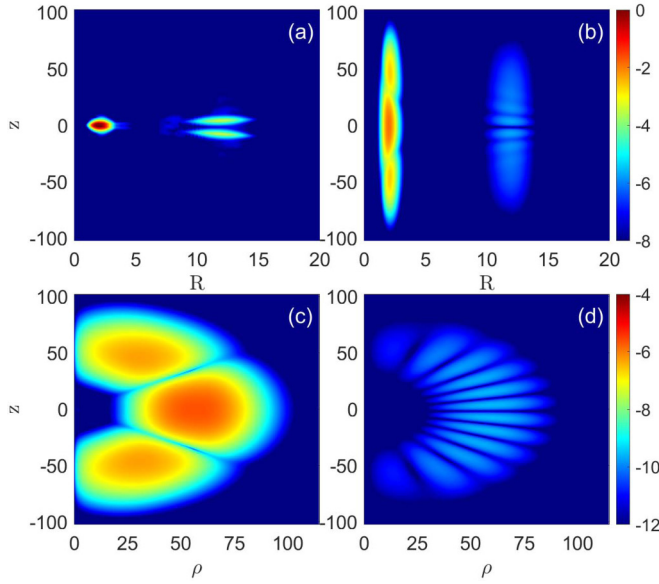
FIG. 2. Spatial wave-function distributions (in logarithmic scale) in the z-R plane (upper row) and in the z-ρ plane (lower row) at the end of the propagation. (a) $\Lambda = 0$ and ρ has been integrated out. (b) $\Lambda = -1$ and ρ has been integrated out. (c) $\Lambda = -1$ and $R = 2$. (d) $\Lambda = -1$ and $R = 12$. The laser parameters are $\omega_1 = 0.6$, $\omega_2 = 5.0$, $\tau_1 = 20$ optical cycles, $\tau_2 = 24$ optical cycles, $E_1 = 0.005$, $E_2 = 3.5$, $\Delta t = 280 + \tau_1$. All quantities are in atomic units.

FIG. 3. The JMS (in logarithmic scale) of the dissociation ionization of (a) HD$^+$, (b) HT$^+$, both normalized to their individual maximum. The corresponding asymmetry parameters defined in Eq. (9) are shown in (c) and (d) for HD$^+$ and HT$^+$, respectively. The laser parameters are the same as those used in Fig. 2. k_z and k_R are in atomic units.

1200, $N_\rho = 460$, $N_z = 1140$ are sufficient to yield convergent results. The time step of short-time evolution is 0.01.

Figures 2(a) and 2(b) show the wave-function distribution in the R-z space while ρ is integrated out for $\Lambda = 0$ and $\Lambda = -1$, respectively. In the pump step, the linearly polarized laser field initiates the molecular dissociation and Λ remains to be zero. After absorbing a circularly polarized photon from the probe pulse, the ionized molecular wave packet mainly resides in the state of $\Lambda = -1$. The minor ionization events induced by the pump pulse are not shown in Fig. 2(b). Figures 2(c) and 2(d) display the R-sliced wave-function distributions in the ρ-z plane corresponding to the two separated parts of ionized wave packets in Fig. 2(b), respectively. Distinct double-slit interference structures are presented in Figs. 2(c) and 2(d). At first glance, the ionization yield at $R = 2$ is much larger than that at $R = 12$. However, they are irrelevant for the purposes of reconstructing the velocity of nuclei in the dissociation. Luckily, they are distinguishable from the interested parts, since their KER in the Coulomb explosion after absorbing the probe photons is quite different. We will then concentrate on the signals in Fig. 2(d) in the rest of this Letter. We also mention that we adopt a very strong probe pulse only to obtain sufficient ionization wave packets at $R = 12$ to stand against the numerical error.

To obtain the JMS of dissociation-ionization events, an assumption is adopted: The Coulomb interaction between the energetic ionized electron and the nuclei is negligible such that the scattering states of the full system are approximated by the product of the electronic plane wave and the nuclear scattering state of the one-dimensional $1/R$ potential. Accordingly, we Fourier transform $u_\Lambda(R, \rho, z; t_f)$ with respect to z
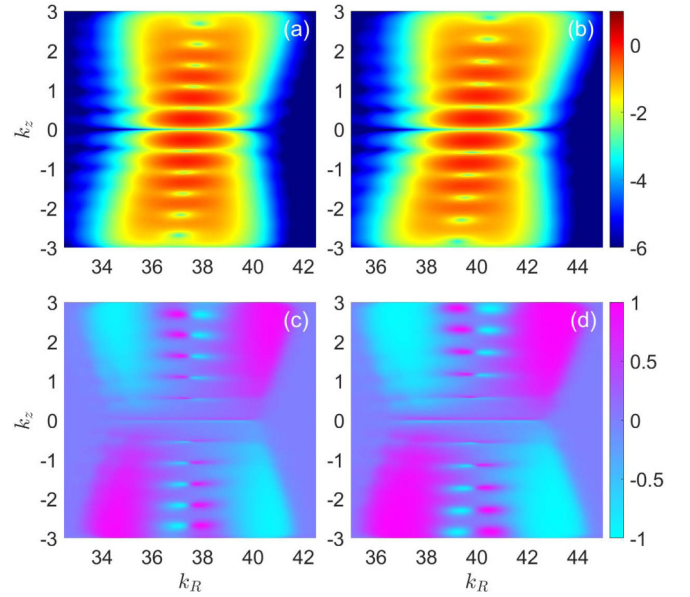
at the end of the simulation $t = t_f$ to obtain $\tilde{u}_\Lambda(R, \rho, k_z; t_f)$, which is then projected to the Coulomb wave function [28] to reach $\tilde{u}_\Lambda(k_R, \rho, k_z; t_f)$. Here, k_z and k_R should be recognized as the asymptotic momenta. The JMS is expressed as

$$\mathcal{P}_\Lambda(k_R, k_z) = \int |\tilde{u}_\Lambda(k_R, \rho, k_z; t_f)|^2 \rho \, d\rho. \tag{8}$$

In principle, the ultimate JMS should summarize contributions from all Λ terms. However, in this work, only the $\Lambda = -1$ term is important. Figures 3(a) and 3(b) show the JMS by using the targets of HD$^+$ and HT$^+$, respectively. During ionization, the electron may escape from either nucleus by forming a double-slit interference pattern, presented as equal-spaced horizontal stripes. The upper and lower halves in Figs. 3(a) and 3(b) show asymmetric distributions. The upper part leans towards the right-hand side. Such asymmetry is more distinct if the nuclear masses differ more. To describe the asymmetric distribution, we define the k_z- and k_R-dependent parameters,

$$\mathcal{A}(k_R, k_z) = \frac{\mathcal{P}_{-1}(k_R, k_z) - \mathcal{P}_{-1}(k_R, -k_z)}{\mathcal{P}_{-1}(k_R, k_z) + \mathcal{P}_{-1}(k_R, -k_z)}. \tag{9}$$

Figures 3(c) and 3(d) plot $\mathcal{A}(k_R, k_z)$. It is worth pointing out that this asymmetry should not be sensitive to the laser intensity and thus the unavoidable focal-volume intensity average in the experiment will not smear out the interference patterns and the asymmetric structures.

A quantitative model is built to explain the numerical results. In this project, it is a good approximation to assume that the resultant photoelectron momentum distribution of single-photon ionization is proportional to the electronic momentum distribution in the initial state [29]. In our case, the initial

state is a dissociative wave packet launched by the pump pulse. Let X_A, X_B, X_e be the position of each particle. At the dissociation limit of $R = |X_B - X_A|$ approaching infinity, the molecule without external fields can be viewed as two isolated systems being perturbed by their interaction. Hence, the Hamiltonian of the system can be written as

$$H_0 = H_{eA} + H_B + V_{eA,B} = H_{eB} + H_A + V_{eB,A}, \qquad (10)$$

where

$$H_{eN} = -\frac{\nabla_N^2}{2m_N} - \frac{\nabla_e^2}{2m_e} - \frac{1}{|X_e - X_N|},$$

$$H_N = -\frac{\nabla_N^2}{2m_N}, \quad N = A, B. \qquad (11)$$

It is straightforward that the solution to $H_{eN}\Psi_{eN} = E\Psi_{eN}$ is separable into the form

$$\Psi_{eN} = \psi_N(X_e - X_N)\chi_N\left(\frac{m_e X_e + m_N X_N}{m_e + m_N}\right), \qquad (12)$$

where ψ_N is the usual atomic state for an electron attached to N, and χ_N is the state of mass center motion of the eN system. The typical trial wave function for describing the electron by the method of a linear combination of atomic orbitals within BOA and in the body-fixed approximation usually neglects such motion, leading to a separative treatment of electronic and nuclear motion, which is improper in the current work. To get the momentum distribution, the Fourier transform of the comoving atomic orbitals should be performed. By transforming X_A, X_B, X_e back into $R = Re_z$ and $r = xe_x + ye_y + ze_z$ (the molecular mass center is set to 0) and keeping only the lowest-order term of m_e/m_N, we obtain the wave packet in momentum representation

$$\tilde{\Psi}_{eA}(p, P) = \tilde{\psi}_A\left(p + \frac{m_e}{m_A}P\right)\tilde{\chi}_A\left(\frac{m_B}{m_n}p - P\right),$$

$$\tilde{\Psi}_{eB}(p, P) = \tilde{\psi}_B\left(p - \frac{m_e}{m_B}P\right)\tilde{\chi}_B\left(\frac{m_A}{m_n}p + P\right). \qquad (13)$$

Note that p and P are the conjugate momenta of r and R. We will show that the pair of asymmetric leaning structures in Fig. 3 can be explained by the inclusion of the electron momentum in the argument of $\tilde{\chi}_A$ or $\tilde{\chi}_B$ in Eq. (13) through the co-motion with the atomic mass center. For a qualitative analysis, we may assume that the $\tilde{\chi}_A$ ($\tilde{\chi}_B$) distribution describing the atomic mass center motion in the channel $A + B^+$ ($A^+ + B$) is Gaussian and centered at $-Q$ ($+Q$). Also, the photoelectron wave packet at the internuclear distance R_c is approximated as

$$\tilde{\psi}_A(p') = \exp\left\{-ip' \cdot \frac{m_B}{m_n}R_c\right\},$$

$$\tilde{\psi}_B(p') = \exp\left\{+ip' \cdot \frac{m_A}{m_n}R_c\right\}. \qquad (14)$$

We plot the momentum distribution for the HD$^+$ given by this simple model in comparison with its BOA degeneration in which the comotion is absent, as shown in Fig. 4. The distributions for ionization from H and D are plotted in Figs. 4(a) and 4(b), respectively. Generally, the molecule is in the superimposed states of $\tilde{\Psi}_{eA}(p, P)$ and $\tilde{\Psi}_{eB}(p, P)$. By coherently adding up them, the asymmetric leaning structures
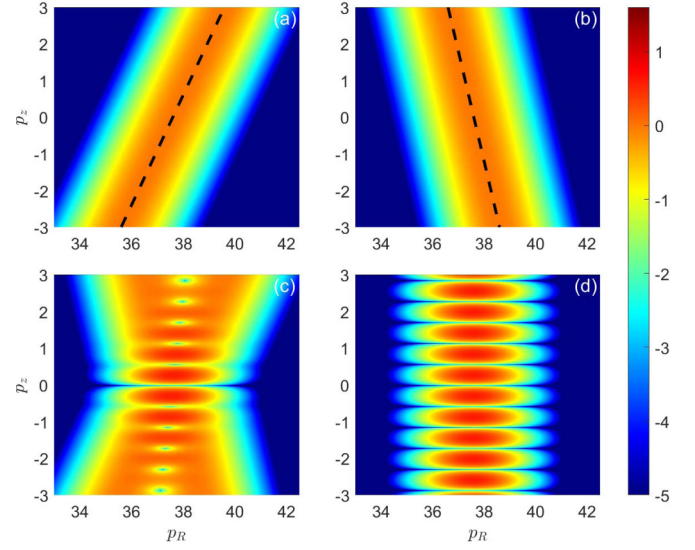

FIG. 4. The momentum distributions given by Eq. (13) in logarithmic scale. (a) $|\tilde{\Psi}_{eA}|^2$. The black dashed line represents the center of Gaussian distribution where $m_B p - m_n P$ remains constant. (b) $|\tilde{\Psi}_{eB}|^2$. The black dashed line represents the center of Gaussian distribution where $m_A p + m_n P$ remains constant. (c) $|\tilde{\Psi}_{eA} - \tilde{\Psi}_{eB}|^2$. (d) The same quantity as (c) but the electron momentum in χ is expelled to follow the BOA. The arbitrarily chosen parameters are $|Q| = 37.6$, $|R_c| = 11$, and the deviation of Gaussian distribution is taken as 1. All quantities are in atomic units.

and the interference patterns are successfully reproduced in Fig. 4(c), while if the comotion is neglected, no leaning structures occur, as shown in Fig. 4(d). It is not strange that although the momenta (p, P) in this model are instantaneous, the distribution in Fig. 4(c) still resembles the one in Fig. 3(a) whose momenta are asymptotic since after the ionization the electron almost decouples with the pair of nuclei and they evolve independently.

In the case where the electron symmetrically localizes on the two nuclei, the electron possesses nonvanishing $\langle p \rangle$ towards the motion of the lighter nucleus, whose value can be approximately estimated by the instantaneous nuclear momentum at ionization,

$$\frac{\langle p \rangle}{m_e} = \left(\frac{1}{m_B} - \frac{1}{m_A}\right)\frac{\langle P \rangle}{2}. \qquad (15)$$

The expected electron momentum can thus serve as a measure of the instantaneous nuclear momentum. A comparison using the electron momentum in the z direction (p_z) and the nuclear momentum in the same direction (p_R) with different targets is presented in Fig. 5 to verify this model. The agreement between the prediction of Eq. (15) and numerical values for HD$^+$ is fairly good, while a small systematic bias occurs in the results of HT$^+$. Besides the numerical error, the main cause of the bias could be due to the mixture of some other electronic states, and the superimposed electronic states cause the electron to have nonzero p_z. Please note that applying the simple mapping in Eq. (15) to where the single active electron approximation fails should be done carefully since it has not been generalized to the situation where multiple electron configurations are important.
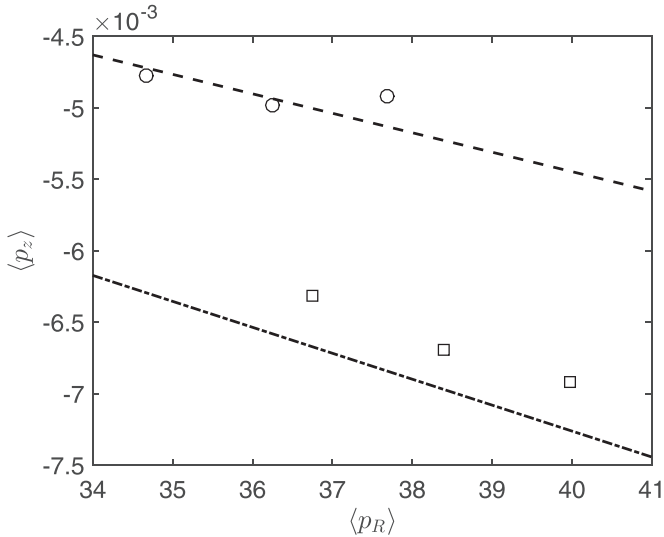
FIG. 5. The averaged momentum transfer to the electron $\langle p_z \rangle$ plotted as a function of $\langle p_R \rangle$. The discrete data marked by circles and squares indicate ($\langle p_R \rangle$, $\langle p_z \rangle$) pairs extracted from the numerical solutions of HD^+ and HT^+, respectively, by implementing different laser parameters. The dashed and dotted-dashed curves are the predicted values from Eq. (15). The laser parameters used here are $E_1 = 0.005$, $E_2 = 3.5$, $\omega_2 = 5.0$, $\tau_1 = 20$ optical cycles, $\tau_2 = 24$ optical cycles, $\Delta t = 280 + \tau_1$. ω_1 has been set as 0.6, 0.65, and 0.7 for three circles and three squares from left to right. All quantities are in atomic units.

In the above analysis, the nonzero $\langle p_z \rangle$ is induced by asymmetric nuclear movement, which is a purely non-BOA effect. Experimentally, besides the above calculated $\langle p_z \rangle$, the photon momentum may transfer to a photoelectron [30,31], contributing the momentum shift along the molecular axis termed as the nondipole effect. To experimentally disentangle the non-BOA effect from the nondipole effect, one may design two

experiments by propagating the laser pulse in two opposite directions [32]. By averaging the photoelectron momentum distributions obtained with the two propagation directions, the nondipole effect is smeared out, and the expected nonzero $\langle p_z \rangle$ is only contributed by the non-BOA effect.

Although in our numerical analysis the molecular axis is parallel to the laser polarization axis, the procedures of alignment are unnecessary in practical experiments which adopt coincident measurements. Among all the experimental data gathered by the detector, one may pick out the nuclei which dissociate or explode into particular directions [33,34]. By postselecting the "correct" dissociative fragments, one may well reconstruct the instantaneous nuclear velocity and instantaneous molecular bond length.

To summarize, by triggering the dissociation of HD^+ with an attosecond pulse, and ionizing the dissociating HD^+ with another time-delayed attosecond pulse, the delay-dependent photoelectron momentum distribution can be recorded. The photoelectron momentum along the laser polarization direction carrying the Young's double-slit interference can be used to extract the internuclear distance at ionization, and the expected photoelectron momentum along the molecular axis can be used to retrieve the instantaneous nuclear velocity. The asymmetrical photoelectron momentum distribution induced by the asymmetrical nuclear movement can be regarded as a mass-polarization effect. One may expect to see this effect in general chemical reactions of heteronuclear molecules.

[1] F. Krausz and M. Ivanov, Rev. Mod. Phys. **81**, 163 (2009).

[2] M. Nisoli, P. Decleva, F. Calegari, A. Palacios, and F. Martín, Chem. Rev. **117**, 10760 (2017).

[3] V. Roudnev, B. D. Esry, and I. Ben-Itzhak, Phys. Rev. Lett. **93**, 163601 (2004).

[4] F. He, C. Ruiz, and A. Becker, Phys. Rev. Lett. **99**, 083002 (2007).

[5] M. F. Kling, Ch. Siedschlag, A. J. Verhoef, J. I. Kkan, M. Schultze, Th. Uphues, Y. Ni, M. Uiberacker, M. Drescher, F. Krausz, and M. J. J. Vrakking, Science **312**, 246 (2006).

[6] G. Sansone, F. Kelkensberg, J. F. Pérez-Torres, F. Morales, M. F. Kling, W. Siu, O. Ghafur, P. Johnsson, M. Swoboda, E. Benedetti, F. Ferrari, F. Lépine, J. L. Sanz-Vicario, S. Zherebtsov, I. Znakovskaya, A. L'Huillier, M. Yu. Ivanov, M. Nisoli, F. Martín, and M. J. J. Vrakking, Nature (London) **465**, 763 (2010).

[7] H. Ibrahim, C. Lefebvre, A. D. Bandrauk, A. Staudte, and F. Légaré, J. Phys. B: At., Mol. Opt. Phys. **51**, 042002 (2018).

[8] P. H. Bucksbaum, A. Zavriyev, H. G. Muller, and D. W. Schumacher, Phys. Rev. Lett. **64**, 1883 (1990).

[9] S. Baker, J. S. Robinson, C. A. Haworth, H. Teng, R. A. Smith, C. C. Chirilă, M. Lein, J. W. G. Tisch, and J. P. Marangos, Science **312**, 424 (2006).

[10] A. Staudte, D. Pavičić, S. Chelkowski, D. Zeidler, M. Meckel, H. Niikura, M. Schöffler, S. Schössler, B. Ulrich, P. P. Rajeev, Th. Weber, T. Jahnke, D. M. Villeneuve, A. D. Bandrauk, C. L. Cocke, P. B. Corkum, and R. Dörner, Phys. Rev. Lett. **98**, 073003 (2007).

[11] B. Manschwetus, T. Nubbemeyer, K. Gorling, G. Steinmeyer, U. Eichmann, H. Rottke, and W. Sandner, Phys. Rev. Lett. **102**, 113002 (2009).

[12] J. Wu, M. Kunitski, M. Pitzer, F. Trinter, L. Ph. H. Schmidt, T. Jahnke, M. Magrakvelidze, C. B. Madsen, L. B. Madsen, U. Thumm, and R. Dörner, Phys. Rev. Lett. **111**, 023002 (2013).

[13] L. He, Q. Zhang, P. Lan, W. Cao, X. Zhu, C. Zhai, F. Wang, S. Wenjing, L. Muzi, X. B. Bian, P. Lu, and A. D. Bandrauk, Nat. Commun. **9**, 1108 (2018).

[14] Th. Ergler, A. Rudenko, B. Feuerstein, K. Zrost, C. D. Schröter, R. Moshammer, and J. Ullrich, Phys. Rev. Lett. **97**, 193001 (2006).

[15] T. Zuo, A. D. Bandrauk, and P. B. Corkum, Chem. Phys. Lett. **259**, 313 (1996).

[16] S. X. Hu and L. A. Collins, Phys. Rev. Lett. **94**, 073004 (2005).

[17] M. Meckel, D. Comtois, D. Zeidler, A. Staudte, D. Pavičić, H. C. Bandulet, H. Pépin, J. C. Kieffer, R. Dörner, D. M. Villeneuve, and P. B. Corkum, Science **320**, 1478 (2008).

[18] J. Xu, C. I. Blaga, K. Zhang, Y. H. Lai, C. D. Lin, T. A. Miller, P. Agostini, and L. F. DiMauro, Nat. Commun. **5**, 4635 (2014).

[19] R. Sun, X. Lai, S. Yu, Y. Wang, S. Xu, W. Quan, and X. Liu, Phys. Rev. Lett. **122**, 193202 (2019).

[20] A. González-Castrillo, A. Palacios, H. Bachau, and F. Martín, Phys. Rev. Lett. **108**, 063009 (2012).

[21] M. J. J. Vrakking, Phys. Rev. Lett. **126**, 113203 (2021).

[22] K. Sändig, H. Figger, and T. W. Hänsch, Phys. Rev. Lett. **85**, 4876 (2000).

[23] T. Barillot, P. Matia-Hernando, D. Greening, D. Walke, T. Witting, L. Frasinski, J. Marangos, and J. Tisch, Chem. Phys. Lett. **683**, 38 (2017).

[24] J. Duris, S. Li, T. Driver, E. G. Champenois, J. P. MacArthur, A. A. Lutman, Z. Zhang, P. Rosenberger, J. W. Aldrich, R. Coffee, G. Coslovich, F. Decker, J. M. Glowinia, G. Hartmann, W. Helml, A. Kamalov, J. Knurr, J. Krzywinski, M. Lin, J. P. Marangos *et al.*, Nat. Photonics **14**, 30 (2020).

[25] M. R. Hermann and J. A. Fleck, Jr., Phys. Rev. A **38**, 6000 (1988).

[26] J. Crank and P. Nicolson, Proc. Cambridge Philos. Soc. **43**, 50 (1947).

[27] R. Kosloff and D. Kosloff, J. Comput. Phys. **63**, 363 (1986).

[28] I. J. Thompson and A. R. Barnett, J. Comput. Phys. **64**, 490 (1986).

[29] H. R. Reiss, Phys. Rev. A **22**, 1786 (1980).

[30] D. Lao, P. L. He, and F. He, Phys. Rev. A **93**, 063403 (2016).

[31] S. Grundmann, D. Trabert, K. Fehre, N. Strenger, A. Pier, L. Kaiser, M. Kircher, M. Weller, S. Eckart, L. Ph. H. Schmidt, F. Trinter, T. Jahnke, M. S. Schöffler, and R. Dörner, Science **370**, 339 (2020).

[32] A. Hartung, S. Echart, S. Brennecke, J. Rist, D. Trabert, K. Fehre, M. Richter, H. Sann, S. Zeller, K. Henrichs, G. Kastirke, J. Hoehl, A. Kalinin, M. S. Schöffler, T. Jahnke, L. Ph. H. Schmidt, M. Lein, M. Kunitski, and R. Dörner, Nat. Phys. **15**, 1222 (2019).

[33] A. Staudte, S. Patchkovskii, D. Pavičić, H. Akagi, O. Smirnova, D. Zeidler, M. Meckel, D. M. Villeneuve, R. Dörner, M. Yu. Ivanov, and P. B. Corkum, Phys. Rev. Lett. **102**, 033004 (2009).

[34] M. Magrakvelidze, F. He, S. De, I. Bocharova, D. Ray, U. Thumm, and I. V. Litvinyuk, Phys. Rev. A **79**, 033408 (2009).